Effect of Nanocrystalline and Ti Implantation on the Oxidation Behaviour of $Fe_{80}Cr_{20}$ Alloy and Commercial Ferritic Steel

D. Sebayang[1,a], DENI S. Khaerudini[1,b], H. Saryanto[1], M.A. Othman[1], T. Sujitno[2], and P. Untoro[2,c]

[1]Advanced Manufacturing and Materials Center (AMMC),
Faculty of Mechanical and Manufacturing Engineering, University Tun Hussein Onn Malaysia, 86400, Batu Pahat, Johor, Malaysia

[2]Center for Technology of Nuclear Industry Material,
National Nuclear Energy Agency (BATAN), Kawasan Puspiptek Serpong Gd.43 Tangerang 15314, Banten, Indonesia

[a]darwin@uthm.edu.my, [b]seadick2000@yahoo.com, [c]untoro@batan.go.id,

Keywords: Nanocrystalline, $Fe_{80}Cr_{20}$, Ion Implantation, Titanium, Oxidation, Microstructure

Abstract. The oxidation behaviour of developed $Fe_{80}Cr_{20}$ alloy and commercial ferritic steel at 1173 - 1373 K in air is studied. Effects of crystallite size and titanium implantation on the oxidation behaviour of specimens were analyzed based on oxide morphologies and microstructures. Oxide scales characterisations of specimen after oxidized were identified by X-ray diffraction (XRD). The surface morphology of oxide scales were examined with scanning electronic microscope (SEM) and energy dispersive X-ray analysis (EDX). The rate constant of oxidation were determined using Wagner method. The results show that crystallite size and titanium implantation has remarkably enhanced the oxidation resistance. The oxidation kinetics indicate that the developed $Fe_{80}Cr_{20}$ as the finer crystallite size both unimplanted and implanted specimens show better performance.

Introduction

The interconnect is a critical component in the stack of solid oxide fuel cells (SOFC), which act as a physical separation between anode and cathode gases and provide the electronic connection between the single cells of the stack. Technical requirements to be used as interconnect in SOFC should fulfil a number of specific requirements, i.e. a high oxidation resistance, a high electrical conductivity of the surface oxide scales, gas tightness, and a coefficient of thermal expansion matched to the electrolyte and the electrodes [1,2]. Cr based alloys and high-Cr ferritic steels seem to be the most promising metallic interconnect materials. For these reasons, the interconnect is a key element for the functioning and long-term reliability of SOFC.

The heat-resistance alloys preferred exhibit superior oxidation resistance; since they are subjected to severe temperature fluctuations, which its oxidation kinetics characteristic usually follows a parabolic rate law [3]. The extensive oxide losses from the surface or oxide spalling has become a serious challenge that leading to serious deterioration of the cell performance [4]. Application of two classes of technology can be used to reduce the growth rate of the oxide scale [5]. The first is to develop new alloys and the other is to conduct surface modifications. In order to develop new alloys, the strength and corrosion resistance of alloy can be improved by crystallite size refinement, especially to nanometric scale [6]. It has been reported that nanocrystalline exhibit a variety of previously unavailable properties including surface reactivity [7]. Other technology, surface treatment with ion implantation widely used to modify the oxidation behaviour and surface mechanical properties of metals [8]. It has been known that relatively minor additions of oxygen active element, such as La, Y, and Ce, could significantly improve the resistance of the oxide scales growth [9]. Previous study [10] has been performed to investigate the effect of reactive elements Ce and Y that clearly improves high temperature oxidation behaviour of developed FeAl alloy by ion implantation. The protection of high temperature alloys and implantation against oxidation is provided by the formation of slow growing oxide films, which often consist of alumina or chromia.

Numerous types of alloys have been examined as candidates for interconnects in SOFC [11]. It has shown that the commercial ferritic steels still need further modification due to possess the suitable properties required for long-term reliable cell performance. To enhance the oxidation resistance, the nanocrystalline $Fe_{80}Cr_{20}$ alloys were developed and surface treated with ion implantation method. Therefore, in this paper studies the effect of nanocrystalline structure and Ti implantation of the alloys on the oxidation behaviour due to prevent the deleterious and fast growing of oxide exposed at 1173-1373 K in air. The oxidation behaviour of as developed $Fe_{80}Cr_{20}$ alloy will be discussed in detail and compared with the as received commercial ferritic steels accordingly.

Materials and Experimental Procedure

The chemical compositions of the studied alloys: as developed $Fe_{80}Cr_{20}$ alloys with nominal Cr content of 20 wt% were prepared by mechanical alloying with different milling time 40, 60, and 80 h, and continued with hot press. The detail processes were reported in previous study [12]. The as received commercial ferritic steel, containing 14.5 wt% Cr as main alloying elements and 1.07 wt% Si, 0.51 wt% Mn, 0.42 wt% C, 0.23 wt% Ni, 0.14 wt% Mo, 0.09 wt% P, 0.03 wt% Cu, 0.02 wt% W, and 0.02 wt% Zr as micro alloying elements were selected for this study. Prior to ion implantation, the selected specimens with the size of surface area of 8 cm^2 were ground with #1500 grit SiC sand paper, polished with 0.05 μm diamond paste, ultrasonically cleaned in ethanol for 30 min, rinsed with deionised water, and dried. The implantation of reactive element of Ti ions were produced at a nominal dose of $1x10^{17}$ ions/cm^2, ion beam energy of 100 keV, pulsed high voltage of 200 kV, and beam current density of 10 μA/cm^2. The average crystallite size of specimens were calculated and found to be 53.33, 38.51, 76.60, and 77.30 nm for $Fe_{80}Cr_{20}$ 40, 60, 80 h, and commercial ferritic steel, respectively. The detail explanations of crystallite sizes evaluation and calculation have been reported previously [13]. High temperatures oxidation resistance for unimplanted and implanted specimens were tested in laboratory air at atmospheric pressure in a PROTHERM box furnace; exposed at 1173 - 1373 K for 100 h and interrupted every 20 h for mass gain measurement on a microbalance with a weighting accuracy of 0.01 mg. The heating and cooling rates were 5 ^oC/min. The measurement of the oxidation resistance is applied the mass gain evaluation. After oxidized for certain time (t) and temperature, the specimens are cooled to room temperature. The mass gain resulted from mass gain per unit surface area of specimen that can be calculated by: $y(t) = (W_t - W_0)/A$, in this function, W_0, W_t, and A, respectively, represent the initial mass, oxidized mass after oxidation for (t) hours and the initial surface areas of the samples. The parabolic rate law was also usually considered as the basis for data processing and interpretation of oxidation resistance [3]. At high temperature, the square of specific area mass gain caused by oxidation increases linearly with the oxidation time, satisfying the diffusion-controlled parabolic kinetics law as: $(\Delta W/A)^2 = k_p t$; where k_p is the parabolic rate constant which determined by the slope of a linear regression-fitted line of mass gain per unit surface area of a specimen $(\Delta W/A)^2$ vs. exposure oxidation time (t) plot. After oxidation, the oxide scales of specimens were identified by the use of BRUKER D8 Advance XRD. The surface morphology of the oxidised specimens and scales were conducted using a JEOL JSM-6380 SEM/EDX.

Results and Discussion

Figs. 1a, b, and c show the mass gain curves of the studied alloys with different crystallite size and implantation oxidized at 1173, 1273, and 1373 K, respectively. Mass gain curves indicate that commercial ferritic steel displayed higher mass gain trend and exhibits poor oxidation resistance. The mass gains of commercial ferritic steel were obtained 59.00, 197.29, and 214.57 mg/cm^2, respectively. Meanwhile, the mass gains of implanted $Fe_{80}Cr_{20}$-38.51 nm were only 12.58, 19.71, and 164.24 mg/cm^2 at 1173, 1273, and 1373 K, respectively. The mass gains of unimplanted $Fe_{80}Cr_{20}$-38.51 nm were 7.73, 15.43, and 145.82 mg/cm^2 at 1173, 1273, and 1373 K, respectively. The implantations on $Fe_{80}Cr_{20}$-38.51 nm not remarkably change the oxidation rate. It shows slightly higher than unimplanted specimens. However, the mass gain of $Fe_{80}Cr_{20}$-38.51nm tended to be

stable and still show the lowest. Meanwhile, the mass gains of implanted ferritic steel-77.30 nm show an improvement with respect to reducing oxidation at 1173, 1273, and 1373 K compared to the unimplanted were 53.57, 164.38, and 207.14 mg/cm^2, respectively.

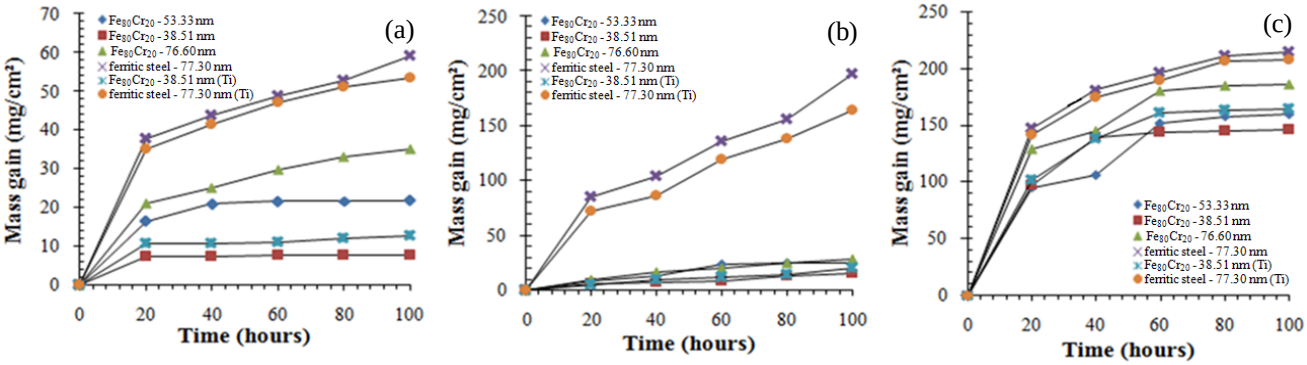

Fig. 1 Mass gain of specimens oxidized at (a) 1173 K, (b) 1273 K, and (c) 1373 K.

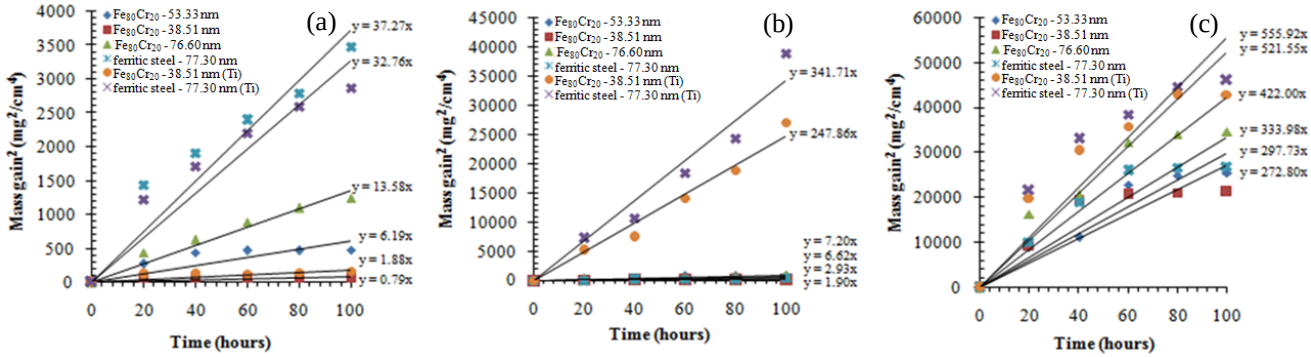

Fig. 2 Parabolic plot of specimens oxidized at (a) 1173, (b) 1273, and (c) 1373 K.

Figs. 2a, b, and c show slope of the straight line of the parabolic rate law as a function of time for specimens oxidized at 1173, 1273, and 1373 K, respectively. The plots show the different scale due to the quite different mass gain in the alloys over exposure temperatures. The smallest parabolic rate constant (k_p) is observed to the smallest crystallite size of $Fe_{80}Cr_{20}$-38.51 nm. The implanted ferritic steel-77.30 nm show lower k_p over exposure temperatures compared to unimplanted specimen; indicating low oxidation rates. Such reduction in the oxidation rate confirmed that the Ti ion implantation was more effective in improving the oxidation resistance of the commercial ferritic steel. Meanwhile, the implanted $Fe_{80}Cr_{20}$ 60 h slightly higher than unimplanted specimen. The higher oxidation rate is believed to be caused by the formation of volatile oxides which can affect by inward diffusion of Ti implantation to the surface of alloy. A further factor which has to be considered in evaluating the growth rates is that the scales are not completely gastight due to the damage induced by ion implantation process onto the alloy surface, generating localised defects in the $Fe_{80}Cr_{20}$ structure. However, the reason behind this phenomenon still needs to be further explored. The parabolic rate constant of developed specimen at 1173 and 1273 K (Figs. 2a and b) were clearly significant show the different improvement of oxidation kinetics which is up to factor of 10 lower; while at 1373 K (Fig. 2c), it is only as much as factor of 2 lower compared to that as received alloy. From the present study, the compliance of mass gain and parabolic rate indicates that oxidation reaction consider due to the crystallite size and reactive element implantation.

The XRD patterns of specimens in different crystallite sizes and implantation oxidized at 1173 K are showed in Fig. 3. In Fig. 3a, it shows the gradually increase of XRD peaks intensity obtained on unimplanted specimens. The peaks corresponding to the alloy crystallite size show a significant intensity in the Bragg peaks. The peak intensity of $Fe_{80}Cr_{20}$-38.51 nm as the finer crystallite size appears the relative lower peaks intensity. In contrary, the intensity of commercial ferritic steel as the coarser crystallite size shows the highest peaks. This intensity corresponds to the oxide scales growth of the alloy substrate during high temperature oxidation. The major phases of oxide scales

are identified $(Fe,Cr)_2O_3$, Fe_2O_3, and Cr_2O_3. The growing oxide peaks on the $Fe_{80}Cr_{20}$ alloys were detected the original FeCr phase. It indicates that the oxide growth on the surface of developed alloy occurred but still not significant, as confirmed by less k_p (Fig. 2a). Fig. 3b shows the XRD diffractograms obtained for the titanium-implanted specimens. It is also shows the significant different peak intensity between the implanted $Fe_{80}Cr_{20}$-38.51 nm and the commercial ferritic steel. The scales formed on implanted specimens were mainly composed of $(Fe,Cr)_2O_3$, Fe_2O_3, Cr_2O_3, and minor phase of TiO_2. The titanium implantation induced preferential nucleation of Cr_2O_3 by an enhanced transport of chromium to the alloy surface. Meanwhile, on unimplanted specimens Fe_2O_3 was observed as major component. The diffractogram also reveal that the appearance of $(Fe,Cr)_2O_3$ and Cr_2O_3 phase at exposure oxidations is growing on the specimen surface. It established the effect of the main impurities alloy (Cr) of as developed and received specimens. The iron-containing oxides Fe_2O_3 seems to be the most possible phase, but a possible mixed compound such as $(Fe,Cr)_2O_3$, solid solution of iron oxide and chromia, can also be envisaged. The scales formed on specimens oxidized at 1273 and 1373 K also show the same phenomena in the scales compositions and peaks trend due to the crystallite size and implantation. However, the significant differences are in the peaks intensity obtained gradually increasing due to the higher oxidation temperature and the FeCr phase for the developed alloys was no longer appeared

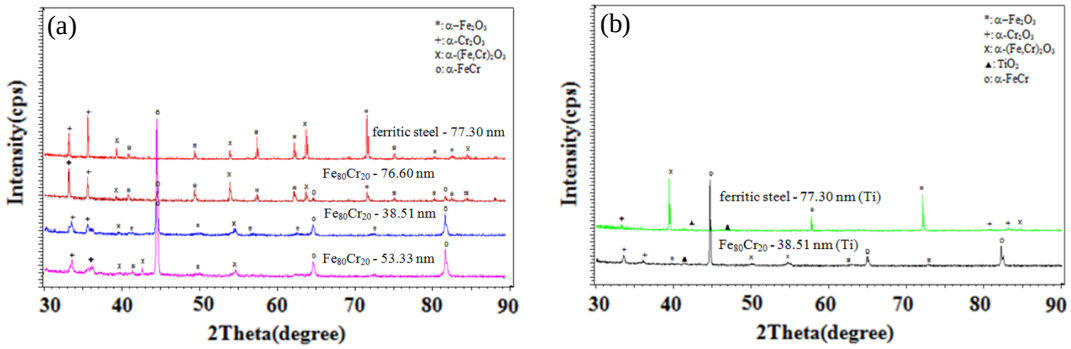

Fig. 3 X-rays diffractograms of (a) unimplanted and (b) implanted specimens oxidized at 1173 K.

Fig. 4 (a-f) show the surface morphology of oxide scale on the specimens after oxidized at 1173 K. The surfaces of $Fe_{80}Cr_{20}$-53.33 and 38.51 nm were covered with compact oxide scale consisting of fine grain scales (Fig. 4a and b). The oxide scales showed that the mainly consisted of chromia. This occurrence can be explained due to chromia growth mechanism, where chromium preference diffused outward to react with oxygen. The $Fe_{80}Cr_{20}$-38.51 nm show better promoting the formation

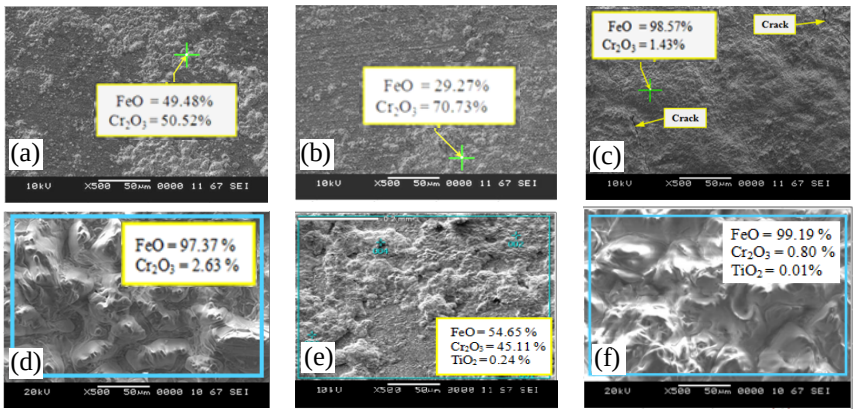

Fig. 4 Surface morphology of specimens oxidized at 1173 K: (a) $Fe_{80}Cr_{20}$-53.33 nm, (b) $Fe_{80}Cr_{20}$-38.51 nm, (c) $Fe_{80}Cr_{20}$-76.60 nm, (d) ferritic steel-77.30 nm, (e) $Fe_{80}Cr_{20}$-38.51 nm (Ti), and (f) ferritic steel-77.30 nm (Ti).

of Cr_2O_3. The oxide scale that formed on the surface $Fe_{80}Cr_{20}$-76.60 nm indicated covered and distributed evenly with main composition of FeO approximately 98.57 at% (Fig. 4c). The implanted

$Fe_{80}Cr_{20}$ 38.51 nm shows Cr_2O_3 in large amount compositions; this indicated that the outer surface of the Cr_2O_3 was clearly protected by surface treatment of reactive element (Fig. 4e). It also shows the distributed prevalent of oxide scale. For the as commercial ferritic steels show coarser grain scales with the big nodules and spallation across the surface of specimen (Fig. 4d and f), but for the implanted specimen, it show better in finer nodule.

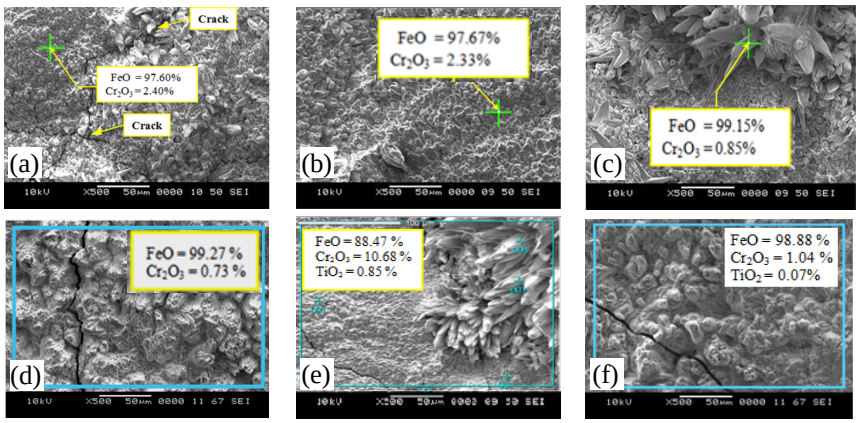

Fig. 5 Surface morphology of specimens oxidized at 1273 K: (a) $Fe_{80}Cr_{20}$-53.33 nm, (b) $Fe_{80}Cr_{20}$-38.51 nm, (c) $Fe_{80}Cr_{20}$-76.60 nm, (d) ferritic steel-77.30 nm, (e) $Fe_{80}Cr_{20}$-38.51 nm (Ti), and (f) ferritic steel-77.30 nm (Ti).

Fig. 5 (a-f) shows the surface of scale formed on the specimens oxidized at 1273 K. The scale on the surface specimen $Fe_{80}Cr_{20}$-53.33 nm indicated fine grained and discontinuous (Fig.5a). It can be explained due to the loose and incompact oxide scale. The oxide scales show mainly consisted of Cr_2O_3 2.40 and FeO 97.60 at%. However, the adherence between oxide scale and a base metal reduced then previous oxidation causes the occurrences of cracks. The oxide scale on $Fe_{80}Cr_{20}$-38.51 nm showed relative stable in more compact scale (Fig.5b). The scales on $Fe_{80}Cr_{20}$-76.60 nm indicated small nodule with a main composition of FeO approximately 99.15 at% (Fig.5c). Due to the loose and incompact oxide scale, obvious cracks and pores were distinguished on commercial ferritic steel (Fig.5d). For the implanted specimen show better oxide scale indicated in the finer of oxide scale, although the cracking also occur (Fig.5f). Meanwhile, the scale of implanted $Fe_{80}Cr_{20}$-38.51 nm exhibit better in oxide morphology (Fig.5e).

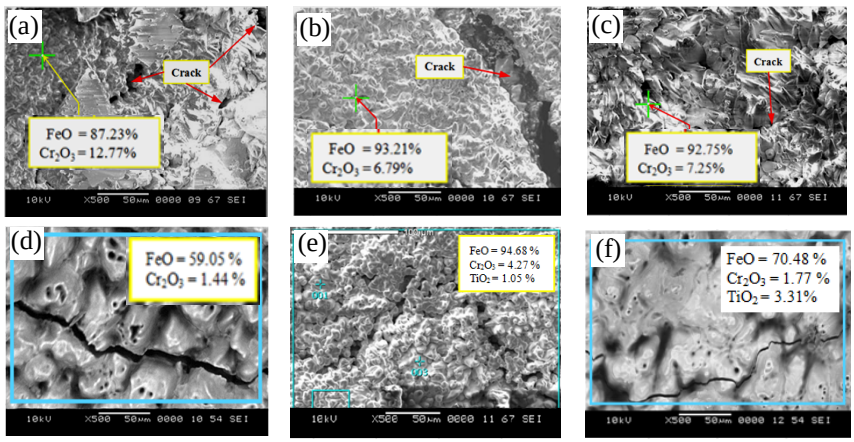

Fig. 6 Surface morphology of specimens oxidized at 1373 K: (a) $Fe_{80}Cr_{20}$-53.33 nm, (b) $Fe_{80}Cr_{20}$-38.51 nm, (c) $Fe_{80}Cr_{20}$-76.60 nm, (d) ferritic steel-77.30 nm, (e) $Fe_{80}Cr_{20}$-38.51 nm (Ti), and (f) ferritic steel-77.30 nm (Ti).

At 1373 K, the oxide formed on the surface of specimens is shown in Figs. 6 (a-f). It indicated the relatively larger concentration of FeO. The formation of iron rich oxides beneath a dense chromia scale may occur if the chromia scale becomes unstable in the equilibrium with the chromia.

The instability of chromia has led to the increasing growth of FeO, due to the loose and incompact scale thus causing the crack in the surface of specimen. The outer scale was easy to peel off and decomposed during further oxidation. The decomposed product oxygen may diffuse to the oxidation/alloy interface through the cracks and pores in the oxide scale. The outward diffusion of metallic ions dominated the development of the outer oxide scales. The Cr element, diffused and agglomerated outward to the scale surface, then part of it directly oxidized with O and partly substituted the Fe in FeO. This could be clearly proven by XRD patterns in Fig. 3 which plotted the increase of $(Fe,Cr)_2O_3$ and decrease of Cr_2O_3. It can be noticed that a discontinuous Cr_2O_3 scale was formed but could not protect the alloy from internal oxidation. At the same time, Fe became enriched and diffused outwards which caused the formation and rapid growth of FeO. Blocked by Cr_2O_3, FeO nucleated and grew at the discontinuous areas such as the incompact Cr_2O_3 scale or its micro-defective areas; leading to some bulges and cracks. Surface treatment of the native metal along with controlled oxidation was found to provide a benefit: a significant reduction in oxide scale growth rate.

Conclusions

The nanocrystalline structure increase the oxide scales grown. Dense, protective, and relatively less mass gain is found to the developed alloy with finer crystallite size of $Fe_{80}Cr_{20}$-38.51 nm. The implantation of reactive element Ti considerably reduces the chromium evaporation. However, it well established that nanocrystalline exhibit major influence on the oxidation resistance.

Acknowledgment

The authors acknowledge the funding support of the UTHM through the Fundamental Research Grant Scheme project of the Ministry of Higher Education - Malaysia under vot no 0361 and 0759.

References

[1] W.J. Quadakkers, J.P. Abellan, V. Shemet and L. Singheiser, Mat. High Temp. Vol. 20 (2003), p. 115.

[2] M. Palcut, L. Mikkelsen, K. Neufeld, M. Chen, R. Knibbe and P.V. Hendriksen: Cor. Sci. Vol. 52 (2010), p. 3309.

[3] D.J. Young: *High Temperature Oxidation and Corrosion of Metals* (Elsevier Ltd., UK, 2008).

[4] E. N'Dah, S. Tsipas, M.P. Hierro and F.J. Perez: Cor. Sci., Vol. 49 (2007), p. 3850

[5] C. Collins, J. Lucas, T.L. Buchanan, M. Kopczyk, A. Kayani, P.E. Gannon, M.C. Deibert, R.J. Smith, D.-S. Choi and V.I. Gorokhovsky: J. Surf. & Coat. Tech. Vol. 201 (2006), p. 4467

[6] M. Krasnowski and T. Kulik: Intermetallics Vol. 15 (2007), p. 201

[7] C.Suryanarayana: J. Progress in Mat. Sci. Vol. 46 (2001), p. 1

[8] G. Marest: J. Hyperfine Interactions Vol. 111 (1998), p. 121

[9] M.A. Montealegre, J.L.G. Carrasco, M.A.M. Munoz, J. Chao, and D.G. Morris, Intermetallics Vol. 8 (2000), p. 439

[10] F.M. Noor, D. Sebayang, P. Untoro: Proc. 9th Intl. Conf. on Quality in Research (2006).

[11] B. Hua, J. Pu, F. Lu, J. Zhang, B. Chi and L. Jian, J. Power Sources Vol. 185 (2008), p. 419

[12] P. Untoro, D. Sebayang, H. Saryanto: Proc. 7th AMC conference (2009).

[13] H. Saryanto, D.S. Khaerudini, P. Untoro, M.H. Saleh, D. Sebayang: Adv. Mat. Res. Vol. 129-131 (2010), p. 999